

DDRF: Denoising Diffusion Model for Remote Sensing Image Fusion

ZiHan Cao^{†1}, ShiQi Cao^{†2}, Xiao Wu¹, JunMing Hou³, Ran Ran¹, and LiangJian Deng^{*1}, *Member, IEEE*

Abstract—Denoising diffusion model, as a generative model, has received a lot of attention in the field of image generation recently, thanks to its powerful generation capability. However, diffusion models have not yet received sufficient research in the field of image fusion. In this article, we introduce diffusion model to the image fusion field, treating the image fusion task as image-to-image translation and designing two different conditional injection modulation modules (i.e., style transfer modulation and wavelet modulation) to inject coarse-grained style information and fine-grained high-frequency and low-frequency information into the diffusion UNet, thereby generating fused images. In addition, we also discussed the residual learning and the selection of training objectives of the diffusion model in the image fusion task. Extensive experimental results based on quantitative and qualitative assessments compared with benchmarks demonstrates state-of-the-art results and good generalization performance in image fusion tasks. Finally, it is hoped that our method can inspire other works and gain insight into this field to better apply the diffusion model to image fusion tasks. Code shall be released for better reproducibility.

Index Terms—Denoising diffusion model, pansharpening, image fusion

I. INTRODUCTION

Pansharpening, as a fundamental problem in remote sensing image fusion processing, it attracts more interest from research community and commercial companies. Pansharpening requires a high spatial resolution panchromatic (PAN) image and a low spatial resolution multispectral (LrMS) image, and fuse two domains together to obtain a high spatial resolution multispectral image (HRMS) which preserves the advantages of the two domains. Most satellites can simultaneously capture PAN and MS images, such as WorldView3 and GaoFen2. Pansharpening can also be seen as a preprocessing method for further high-level applications, such as change detection [1], [2], mineral exploration [3], [4] and segmentation [5].

Pansharpening methods are usually divided into four categories, i.e., component substitution (CS) methods, variational optimized (VO) techniques, multiresolution analysis (MRA) methods and machine learning (ML) approaches. The CS method substitute a component of the LrMS image by the PAN image, contains algorithms such as principal component analysis (PCA) [6], gram-schmidt spectral sharpening [7], [8] and guided filtering [9]. The CS-based methods can generate a fused image with high spatial fidelity but more spectral distortion. The MRA approach extracts features on the spatial dimension from PAN image and then injects them into LrMS

image in a multispectral manner. The representative MRA methods are the additive wavelet luminance proportional (AWLP) [10], smoothing filter-based intensity modulation (SFIM) [11], modulation transfer function (MTF) [12] generalized laplacian pyramid (MTF-GLP) and MTF-GLP with high-pass modulation (MTF-GLP-HPM) [13]. The MRA method preserves better spectral information but suffers from spatial distortion due to its extract-injection manner. The VO-based approaches are recently proposed to address pansharpening issue. Algorithms belonging to this class include Bayesian methods [14], [15], variational methods [16], [17], [18]. VO-based methods fuse better HRMS images owing to their mathematical rigor with respect to the state-of-the-art CS-based and MRA-based methods. However, the performance improvement brings higher computational costs and more tunable parameters.

Over recent years, with the improvement of the hardware and deep learning, convolutional neural networks (CNN) [19], [20] and vision Transformers (ViT) [21], [22] have been proposed and achieved significant advances in image processing, e.g. image classification [19], [21], image denoising [23], image deblur [24], image super-resolution [25] and image fusion [26], [27], [28]. Therefore, those DL-based methods quickly become a powerful tool to handle pansharpening task by giving large-scale training datasets and learn a nonlinear functional mapping from LrMS and PAN to HRMS. PNN [29], as a simple but effective CNN, is firstly proposed to deal with pansharpening task. This architecture is inspired by previous CNN for single image super-resolution [30]. PanNet [31] is proposed to explicitly inject high-passed information from PAN image into the upsampled LrMS image and gains a better performance. He *et al.* [32] proposed a detail injection-based CNN. Deng *et al.* [26] employs a residual network by stacking several residual blocks and another residual path from input to output to let the network learn high-frequency details. Those CNN-based methods are constricted by static kernels, which means the kernels are independent of the input. To alleviate this drawback, a dynamic kernel-generated module in LAGNet [33] is inserted to generate dynamic kernels depending on the input.

Diffusion denoising probability model (DPM), as proposed for unconditional image generation [2], [34], conditional image generation [2], [35], text-to-image generation [36], [37], image-to-image translation [38] and discrete nature language generation [39] tasks, has shown its power providing extra feature details and good generation ability. Another advantage is that DPM owns a more stable training process and merely no mode collapse compared to the GAN-based model. The train-

[†] Equal contribution to this work.

^{*} Corresponding author.

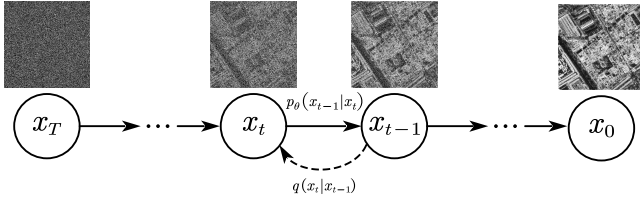


Fig. 1. Denoising diffusion model forward and backward process. $q(\mathbf{x}_t|\mathbf{x}_{t-1})$, $p_\theta(\mathbf{x}_{t-1}|\mathbf{x}_t)$ represent noising adding forward process and denoising backward process, respectively.

ing and testing phase of DPM is dubbed as forward process and backward process [40], [41]. In the forward process, the input image is corrupted by pure Gaussian noise and the model tries to remove the added noise and recover the original input. In the backward process, the input is pure Gaussian noise and the trained model is responsible for removing a little noise step by step, so, after large enough time steps, the input pure noise is recovered to the generated images. To control the generated images, Ho *et al.* [42] propose conditional DPM, the condition is fed into the diffusion model to control the SDE [2], [40], [41] or ODE [43], [44] trajectory.

In this paper, We propose DDRF for pansharpening. Mainstream works on pansharpening often concentrate on model architectures and information gathering operations. Most of them choose to fuse two domains directly and few notice generative models can hallucinate more detailed information as they are trained in a generative manner. Those non-generative models often suffer high-frequency component loss, spectral or spatial distortions. On the contrary, DPM with SDE sampling can introduce new noise that contains many high-frequency components when sampling for better generation. Our contribution can be summarised in the following four folds:

- 1) We firstly propose DDRF for pansharpening, which is a supervised diffusion model but modified to suit fusion tasks and can be also extended to other different modal fusion tasks (e.g. hyperspectral image fusion). While achieving good performance, we hope our DDRF can draw attention to diffusion models in the field of image fusion.
- 2) Two conditional injection modules are designed that are used for injecting conditions in a style transfer manner and a details complemented manner, respectively.
- 3) Our DDRF reaches a new state-of-the-art performance on pansharpening task among three widely used pansharpening datasets and competitive performance on hyperspectral dataset.

II. RELATED WORKS

This section mainly introduces generative and non-generative methods related to pansharpening, as well as mainstream generative tasks and methods related to diffusion models.

A. Non-generative Model

PNN [29] was inspired by the single image super-resolution technique and proposed a convolutional neural network for

pansharpening for the first time. PanNet [31] is proposed to explicitly inject high-passed information from the PAN image into the upsampled LRMS image and gain a better performance. DiCNN [32] is proposed as a details-inject-based CNN which is powerful on frequency details. FusionNet [26] simply employs a residual from the start to the end of the network, explicitly enabling the network to learn the high-frequency details. Due to the static kernel of the conventional convolutional operator, LAGNet [33] with dynamic kernel generated based on input can better fuse two domains. AKD [45] further exploits the idea of LAGNet and proposes two dynamically generated branches responsible for spectral and spatial details extraction, respectively. SpanConv [46] presents an interpretable span strategy, for the effective construction of kernel space and reducing the redundancy of the convolution but still maintaining good performance. PMACNet [47], a parallel convolutional neural network structure, is employed with a pixel-wise attention constraint (PAC) module and a novel multireceptive-field attention block (MRFAB), successfully solved the small receptive field brought by CNN.

B. Generative Model

Generative models, as another promising branch for multi-modal fusion, including GANs, flow-based models, energy-based models, and diffusion models have been proposed from different perspectives and have received a lot of attention and research, leading to the development of various types of generative tasks. Benefiting from the development of these generative models, generative models can also be applied to pansharpening, producing in good results.

GAN-based model is first introduced by Goodfellow *et al.* [48] including a generative model G that generates a sample on the data distribution, and a discriminative model D that estimates the probability that a sample comes from the training data rather than G . The training procedure for G is to maximize the probability of D making a mistake. Through this minmax two-player adversarial training procedure, the generative ability of G is promoted. To deal with the training instability and failure to converge, W-GAN [49] is presented using the Wasserstein distance as the loss function, which provides more accurate gradient information and avoids the gradient vanishing and mode collapse issues during training. Improved W-GAN [50] further provides an alternative to clipping weights: penalize the norm of the gradient of the critic with respect to its input and achieve higher-quality generations. StyleGAN v1 [51] and StyleGAN v2 [52] further push forward the stability and diversity of GAN.

Ma *et al.* [53] firstly introduced GANs into pansharpening and performed unsupervised learning of spectral and spatial information based on the reversed loss function upon the network's output. Zero-GAN [54] also relies on GAN and constructed a non-reference loss function, including an adversarial loss, spatial and spectral reconstruction losses, a spatial enhancement loss, and an average constancy loss to specifically supervise the learning process.

Flow-based model is a type of generative model that learns the underlying distribution of data by transforming a simple

input distribution into the target distribution through a series of invertible transformations. This is achieved by representing the probability density function of the target distribution as a sequence of flows, where each flow is an invertible transformation. Some notable contributions in the field of flow-based models include the Real-valued Non-Volume-Preserving (Real NVP) model, introduced by Dinh *et al* [55], which proposed a flexible and efficient way to construct invertible transformations using neural networks. Another important contribution is Glow [56], which improved upon previous flow-based models by introducing an invertible 1×1 convolutional operation that greatly increased the expressiveness of the model.

Diffusion model are recently proposed for generation including conditional or unconditional generation [2], [34], [40], text-to-image translation [37], [57], image super-resolution [58], image restoration [59], [60] and other high-level image manipulation tasks [61], [62], [38]. Diffusion models can generate images with more details and higher fidelity than the GAN-based model and flow-based model. The advantages of diffusion models include stable training, minimal mode collapse, and the ability to train with only a single mean squared error (MSE) loss. In comparison to GAN-based models, which suffer from instability issues in their adversarial training, and flow-based models, which are limited in their network performance due to the requirement for reversibility, diffusion models are easier to train and design.

Song *et al.* [63] first introduced a score-based model that produces samples via Langevin dynamics using gradients of the data distribution estimated with score matching. Later, Ho *et al.* [2] proposed DDPM from the direction of weighted variational bound, and their equivalence is proven in NCSN [41]. DDIM [43] designed a non-Markov chain sampling process, which accelerated the sampling of diffusion models. DPM-solver [44] simplified the solution to an exponentially weighted integral of the neural network by computing the linear part of the ODE and applying change-of-variable, further accelerating the sampling process. EDM [35] decoupled various design components of the diffusion model and designed a second-order ODE sampler, which further improved the performance of the diffusion model to reach the state-of-the-art performance.

However, diffusion models have not received much attention in remote sensing images. DDPM-CD [64] utilizes diffusion models for landform change detection. Firstly, an unconditional diffusion model is trained on a large dataset, and the features of a specific layer of the diffusion model during the sampling process are used as additional information input to the segmentation head, producing segmentation results. As a result, DDPM-CD has achieved satisfactory performance in the field of landform change detection. Similar to DDPM-CD, Dif-fuse [65] fuses RGB and near-infrared images and has made considerable progress.

III. METHODOLOGY

Our DDRF will be elucidated in the following parts. Firstly, some notations will be explained. Then diffusion denoising model will be briefly reviewed, including the forward and

backward processes, and the simple derivation of the loss function. Subsequently, we will provide a detailed introduction to the architecture of the diffusion model and two types of conditional injection modules. After that, according to the training objective of the diffusion model, we discuss the three choices (i.e., ϵ , \mathbf{x}_0 , and \mathbf{v}). To facilitate faster sampling, we will also discuss how to transform the VP SDE into a faster-sampling ODE while preserving the marginal distribution in the final subsection.

A. Notation

We first clarify the notations. An image of size $\mathbb{R}^{H,W,C}$ represented by a tensor is denoted as \mathbf{x} . After performing t forward diffusion steps, the resulting noisy image is denoted as \mathbf{x}_t . In particular, we denote the PAN image and the upsampled LrMS image of the same size as the PAN image as $\mathbf{P} \in \mathbb{R}^{H \times W \times 1}$ and $\mathbf{M} \in \mathbb{R}^{H \times W \times C}$, respectively. The feature representation of the intermediate layers of a neural network is denoted as \mathbf{f} . The condition that guides the generation process is represented as \mathbf{c} .

B. Diffusion Model

Diffusion models enable generating a realistic image from a normal distribution by reversing a gradual noising process. The diffusion model accomplishes its task in two steps: forward and reverse processes which are illustrated in Fig. 1.

Forward process aims to make the origin image $\mathbf{x}_0 \sim p_{data}(\mathbf{x}_0)$ noisy by a T step Markov chain that gradually converts it to Gaussian distribution. One forward step is defined as,

$$q(\mathbf{x}_t|\mathbf{x}_{t-1}) = \mathcal{N}(\mathbf{x}_t; \sqrt{1 - \beta_t}\mathbf{x}_{t-1}, \beta_t\mathbf{I}), \quad (1)$$

where $t \in [0, T]$ and \mathcal{N} is a Gaussian distribution which mean is $\sqrt{1 - \beta_t}\mathbf{x}_{t-1}$ and standard deviation is $\beta_t\mathbf{I}$. Through the reparameterization trick, the manner we directly get x_t is defined as

$$q(\mathbf{x}_t|\mathbf{x}_0) = \sqrt{\alpha_t}\mathbf{x}_0 + \sqrt{1 - \alpha_t}\epsilon, \quad (2)$$

where $\epsilon \sim \mathcal{N}(0, 1)$ and $\beta_t \in (0, 1)$ is a pre-defined variance schedule in T steps and $\alpha_t = 1 - \beta_t$, $\bar{\alpha}_t = \prod_{i=0}^t \alpha_i$.

We do reverse processes to denoise x_t , following

$$p_\theta(\mathbf{x}_{t-1}|\mathbf{x}_t) = \mathcal{N}(\mathbf{x}_{t-1}; \mu_\theta(\mathbf{x}_t, t), \Sigma_\theta(\mathbf{x}_t, t)), \quad (3)$$

where θ denotes the parameters of the model.

The forward process degrades the data distribution into a standard Gaussian distribution. On the contrary, the reverse process, modeled by a neural network, aims to learn to remove the degradation brought from the forward process, i.e., denoising.

To train a diffusion model, maximizing its variational lower bound (VLB) and it can turn into a simple supervised loss [2] written as,

$$\min_{\theta} L_{simple} = \mathbb{E}[\|\epsilon - \epsilon_\theta(\mathbf{x}_t, t)\|_1], \quad (4)$$

Note that in Eq. 4, the model prediction is added Gaussian noise, but it can also be \mathbf{x}_0 [2] or \mathbf{v} [36]. Some discussions will be made in the ablation study.

After training the model, we can sample data starting a standard Gaussian noise \mathbf{x}_T , and according to Eq. 3, the mean and variance can be computed, following

$$\mu_\theta = \frac{1}{\sqrt{\alpha_t}}(\mathbf{x}_t - \frac{\beta_t}{\sqrt{1 - \bar{\alpha}_t}}\epsilon_\theta(\mathbf{x}_t, t)), \quad (5)$$

$$\Sigma_\theta(\mathbf{x}_t, t) = \frac{1 - \bar{\alpha}_{t-1}}{1 - \bar{\alpha}_t}\beta_t. \quad (6)$$

To this end, \mathbf{x}_{t-1} can be sampled from the previous step. Through T iterative sampling steps, \mathbf{x}_0 can be obtained.

In the image fusion task, there usually are two or even more images from different domains. Take pansharpening as an example, PAN image and LrMS images are from different domains and the HRMS image is from the target domain. We treat the fusion task as an image-to-image translation task. To guide the generation process, we empirically set the LrMS, PAN, and constructed wavelet coefficients (present in sec. III-F) as conditions denoted as \mathbf{c} . Then the forward, the backward distributions and training objective (i.e., Eq. 1-6) shall be conditioned on \mathbf{c} .

C. Deep Model Architecture

As shown in Fig. 2, the overall network architecture of our DDRF is similar to SR3 [58] and is composed of an encoder, decoder, and two middle self-attention modules, which resembles an Unet architecture consisting of convolutional layers. There are two downsampling operations between the two layers of the encoder to reduce spatial resolution and increase the number of channels. Similarly, there is an upsampling operation by a factor of 2 between the two layers of the decoder to increase spatial resolution and reduce the number of channels.

The encoder and decoder have the same number of layers. Differently, the encoder takes in encoded features not only from the previous layer but modulated coarse-grained style condition (seen in sec. III-E). The features of the encoder at the corresponding layer will be concatenated with the input features of the decoder at the corresponding layer and additive wavelet features (seen in sec. III-F) along the channel dimension and fed into the decoder together. Its output can be modeled as added Gaussian noise, \mathbf{x}_0 or \mathbf{v} , which will be discussed in sec. III-G.

D. Residual Learning

Due to the tendency of CNNs to learn low-frequency information, they lack representation of high-frequency information. Previous works have attempted to address this issue by filtering the input with high-pass filters and directly incorporating it as residual input, or by designing specialized high-frequency injection modules and supervising them in the frequency domain. We do not want to design complex high-frequency modules that significantly increase the number of parameters in the network, nor do we want to perform complex operations such as loss computation in the frequency domain.

Inspired by FusionNet [26], we changed the input of the diffusion model during the training process from HRMS to

HRMS – MS and then add noise based on Eq. 2. We found that using residuals as input for HRMS converges faster and produces better results than when HRMS is used as input. Regarding whether to use residual learning or not, discussion and ablation experiments will be shown in sec. IV-I2.

E. Style Transfer Modulation

We concatenate the MS and PAN along the channel dimension and consider it as a conditional input with a style. We inject this conditional input into each layer of the encoder and encode it together with the residual input. We avoid encoding much detailed information in the encoder but reconstructing those in the decoder, to this end, the encoder only needs to consider the overall style, including the approximate information and distribution of both spectral and spatial features.

For such coarse-grained operations, it is feasible to generate the corresponding scale and shift based on the input conditions to modulate the output features of the encoder, which can be represented as,

$$\begin{aligned} \text{scale, shift} &= \text{Split}(\text{MLP}([\mathbf{P}, \mathbf{M}])), \\ \hat{\mathbf{f}} &= \mathbf{f} \cdot (1 + \text{scale}) + \text{shift}, \end{aligned} \quad (7)$$

where `Split` is splitting the feature into two parts with equal size along the channel dimension, $[\cdot]$ represents concatenation along the channel dimension, and $\mathbf{f} \in \mathbb{R}^{h,w,d}$ is the output of the previous decoder layer, $\hat{\mathbf{f}}$ is the modulated output. MLP is implemented as several convolutional layers which are inserted by a SiLU activation in between. $\text{scale} \in \mathbb{R}^{h,w,d}$ and $\text{shift} \in \mathbb{R}^{h,w,d}$ are produced by the MLP. h, w, d are determined by the size of the feature output from the encoder layer.

F. Wavelet modulation

The encoder layer is responsible for encoding spectral and spatial information into a high dimensional and low spatial resolution feature with treating LrMS and PAN as style conditions. The decoder, its objective is to decode high-dimensional, low spatial-resolution features from the encoder as faithfully as possible into the RGB space, using the features learned by the encoder. However, relying solely on the features outputted by the encoder is not sufficient for the decoder. We have found that introducing appropriate high-frequency components during the decoding process is advantageous for producing images with richer details. One intuitive approach is to concatenate the high-frequency components extracted from PAN with the features outputted by the encoder along the channel dimension, and then feed the concatenated features into the decoder for decoding.

We choose to apply wavelet decomposition on the PAN to extract the horizontal, vertical, and diagonal high-frequency components and used a cross-attention mechanism in the decoder to introduce these high-frequency details into the decoding process. However, considering only high-frequency details are insufficient, we also introduced the low-frequency main component of LrMS, which is also extracted using wavelet decomposition similar to PAN. The high-frequency and low-frequency components are concatenated in the channel dimension and then passed through an attention module

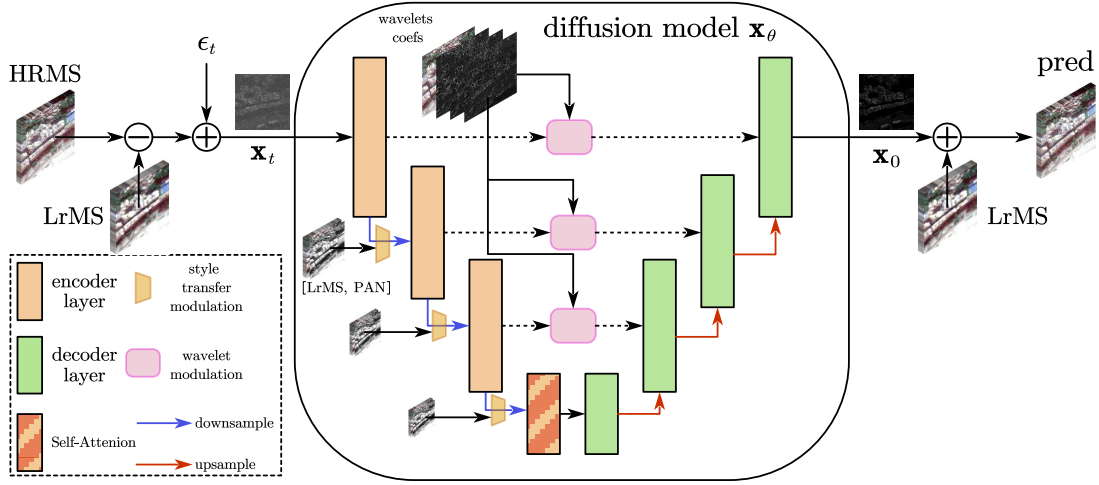


Fig. 2. Framework of our DDRF. The input of DDRF is the residual produced by HRMS subtracted by MS. For simplicity, the time step is omitted. Zooming in for more details.

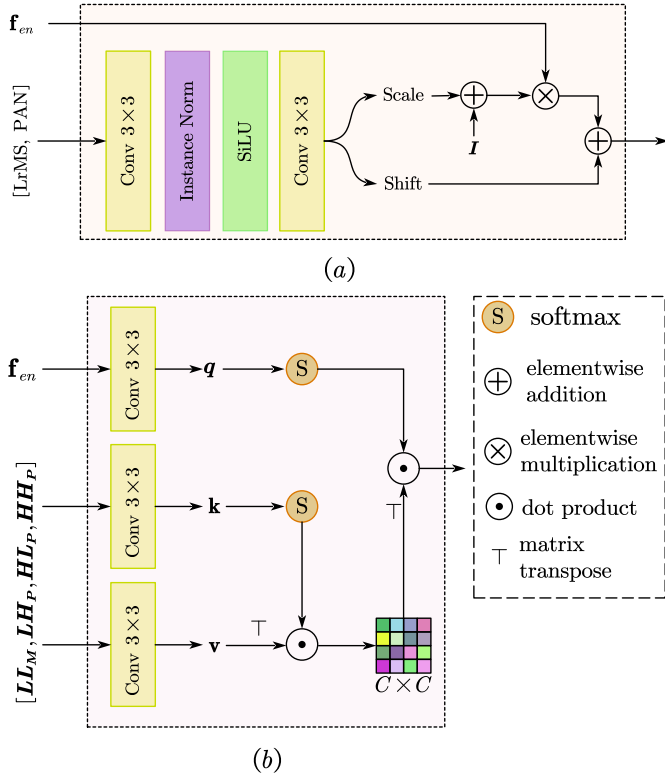


Fig. 3. Two types of modulations. (a) style transfer modulation. (b) wavelet modulation.

with the features outputted by the encoder before being introduced into the decoder. We refer to this process as *Wavelet Modulation*. The advantage of this approach is that it separates the low-frequency and high-frequency components, with PAN providing the high-frequency details and LrMS providing the spectral component, making it easier for the decoder to learn.

To be more specific, we utilized the DB1 wavelet decomposition to decompose both the LrMS and PAN into four components, which include one main component and three detail components in the horizontal, vertical, and diagonal

directions. We can express this process using the following equations,

$$\begin{aligned} \mathbf{LL}_M, \mathbf{LH}_M, \mathbf{HL}_M, \mathbf{HH}_M &= \text{DB1}(\mathbf{M}), \\ \mathbf{LL}_P, \mathbf{LH}_P, \mathbf{HL}_P, \mathbf{HH}_P &= \text{DB1}(\mathbf{P}), \end{aligned} \quad (8)$$

where $\mathbf{LL} \in \mathbb{R}^{C, \frac{H}{2}, \frac{W}{2}}$ denotes the low-frequency main component, and $\mathbf{LH} \in \mathbb{R}^{C, \frac{H}{2}, \frac{W}{2}}$, $\mathbf{HL} \in \mathbb{R}^{C, \frac{H}{2}, \frac{W}{2}}$, and $\mathbf{HH} \in \mathbb{R}^{C, \frac{H}{2}, \frac{W}{2}}$ denote the detail components in the horizontal, vertical, and diagonal directions, respectively.

Since the memory complexity of cross-attention is $\mathcal{O}(n^2)$, where $n = HW$. When approaching the head of the decoder, as the output image size increases, it is unacceptable when dealing with large images due to the quadratic spatial complexity of the image size. we propose a linear-memory cross-attention mechanism to introduce both the high-frequency and low-frequency components into the decoder. We can represent the linear-memory attention mechanism as follows,

$$\begin{aligned} \hat{\mathbf{q}} &= \text{Reshape}(\text{Softmax}(\mathbf{q}, 1)), \\ \hat{\mathbf{k}} &= \text{Reshape}(\text{Softmax}(\mathbf{k}, 2)), \\ \hat{\mathbf{v}} &= \text{Reshape}(\mathbf{v}), \\ \mathbf{A} &= \hat{\mathbf{k}} \cdot \hat{\mathbf{v}}^\top, \\ \mathbf{O} &= \mathbf{A}^\top \cdot \hat{\mathbf{q}}. \end{aligned} \quad (9)$$

As a result, we reduced the memory complexity to $\mathcal{O}(C^2)$, where C is much smaller than n . This significantly reduces memory usage while ensuring the effective introduction of conditions. \mathbf{q} is the output of the corresponding layer in the encoder, and \mathbf{k} and \mathbf{v} are tensors obtained by concatenating the $\mathbf{LL}_M, \mathbf{LH}_P, \mathbf{HL}_P$, and \mathbf{HH}_P components along the channel dimension and then are projected by several convolutional layers as follows,

$$\begin{aligned} \mathbf{q} &= \mathbf{W}_q \otimes \mathbf{f}_{en} + b_q, \\ [\mathbf{k}, \mathbf{v}] &= \mathbf{W}_{k,v} \otimes [\mathbf{LL}_M, \mathbf{LH}_P, \mathbf{HL}_P, \mathbf{HH}_P] + b_{k,v}, \end{aligned} \quad (10)$$

where \otimes is the convolution operation, \mathbf{W} is the weight and b is bias and \mathbf{f}_{en} is the feature from the corresponding encoder layer. The Reshape operation combines the spatial dimensions

of \mathbf{q} , \mathbf{k} , and \mathbf{v} into a single dimension, and can represent as $\text{Reshape} : \mathbf{f} \in \mathbb{R}^{C,H,W} \rightarrow \mathbb{R}^{C,HW}$. $\text{Softmax}(\cdot, i)$ represents applying the softmax operation along the i -th dimension. In this way, the high-frequency details and low-frequency information are injected for better decoding.

G. Training Objective \mathbf{x}_0 , ϵ or \mathbf{v}

There are three choices for the neural network to model, i.e., ϵ , \mathbf{x}_0 , and \mathbf{v} [36]. Note that \mathbf{v} is a combination of the ϵ and \mathbf{x}_0 ,

$$\mathbf{v} = \sqrt{\bar{\alpha}_t}\epsilon - \sqrt{1 - \bar{\alpha}_t}\mathbf{x}_0. \quad (11)$$

In previous diffusion works [2], [34], the training objective is often the added Gaussian noise, which is suitable for large-scale datasets in practice. However, remote sensing datasets are much smaller than those nature image datasets. Intuitively, predicting non-degraded images from noisy images is rather more direct than predicting those added noises. We will show that for small datasets, predicting \mathbf{x}_0 is a better choice than noise and \mathbf{v} in the ablation study.

By turning the objective into \mathbf{x}_0 , we can change this L_{simple} to another loss that has the same form but depends on \mathbf{x}_0 instead. The formula is as follows,

$$L_{\text{simple}} = \mathbb{E}[\|\mathbf{x}_0 - \mathbf{x}_\theta(\mathbf{x}_t, t, \mathbf{c})\|_1]. \quad (12)$$

H. Fast Iterative Sampling

For the backward process, since the diffusion model needs to iterate hundreds or thousands of times to generate an image, this leads to a slow generation speed. To solve this problem, we convert the SDE sampler [2] of the original backward sampling process into an ODE sampler [43], which allows for fast sampling in a non-Markov chain form as

$$\mathbf{x}_{t-1} = \sqrt{\bar{\alpha}_{t-1}}\mathbf{x}_\theta(\mathbf{x}_t, t) + \sqrt{1 - \bar{\alpha}_{t-1} - \sigma_t^2}\epsilon_\theta(\mathbf{x}_t, t), \quad (13)$$

where σ_t is a established function about t and $\mathbf{x}_\theta(\mathbf{x}_t, t)$ is the model prediction of \mathbf{x}_0 , thus we have

$$\mathbf{x}_\theta(\mathbf{x}_t, t) := \frac{\mathbf{x}_t - \sqrt{1 - \bar{\alpha}_t}\epsilon_\theta(\mathbf{x}_t, t)}{\sqrt{\bar{\alpha}_t}}, \quad (14)$$

we can know from Eq. 14 that the sampler predicts \mathbf{x}_0 directly from \mathbf{x}_t and then generates \mathbf{x}_{t-1} through a reverse conditional distribution. Therefore, we can accelerate sampling by $\tau = [\tau_1, \tau_2, \dots, \tau_{\dim(\tau)}]$. Specifically, τ is a subset of $[1, 2, \dots, T]$, and we can make a fast sampling after using τ ,

$$\mathbf{x}_\theta(\mathbf{x}_{\tau_i}, \tau_i) := \frac{\mathbf{x}_{\tau_i} - \sqrt{1 - \bar{\alpha}_{\tau_i}}\epsilon_\theta(\mathbf{x}_{\tau_i}, \tau_i)}{\sqrt{\bar{\alpha}_{\tau_i}}}, \quad (15)$$

so that the sampling speed can be greatly improved.

IV. EXPERIMENTS

A. Experimental Settings

1) *Implementation Details*: our DDRF is implemented in PyTorch 1.13.1 and Python 3.10.9 using AdamW optimizer with a learning rate of 0.0001 to minimize L_{simple} on a Linux operating system with two NVIDIA GeForce RTX4090 GPUs. The initialization of convolution modules is based on a

kaiming initialization. To obtain wavelet coefficients, we use DB1 wavelets decomposition method and decompose the image into four wavelet coefficients. For diffusion denoising model, we choose a cosine schedule [34] for α_t following,

$$\bar{\alpha}_t = \frac{f(t)}{f(0)}, f(t) = \cos\left(\frac{t/T + s}{1 + s} \cdot \frac{\pi}{2}\right). \quad (16)$$

In practice, we set $s = 8e - 3$. The model does not learn the variance term Σ_θ introduced in improved-ddpm [34]. The total training diffusion time step is set to 500 for both pansharpening and hyperspectral fusion experiments. The exponential moving average (EMA) ratio is set to 0.995. The total training iterations for WV3, GF2, QB, and CAVE datasets are set to 100k, 100k, 200k, and 300k iterations, respectively. To reduce the number of sampling steps, according to Eq. 14 and 15, we set the number of sampling steps to 25 for the pansharpening task, and 100 for the hyperspectral image fusion task.

2) *Datasets*: In order to show the effectiveness of our DDRF, we conduct experiments over the widely-used datasets including World-View3 (8 bands), Gao-Fen2 (4 bands), and Quick-Bird (4 bands) datasets.

For **pansharpening datasets**, to best evaluate the performances, we simulate the reduced resolution and full resolution datasets to obtain the reference metrics and non-reference metrics. For the reduced datasets, to obtain the simulated images with ground-truth images, we follow Wald's protocol [66] to get them. It has three steps: 1) Downsample the original PAN and the original MS images by a factor of 4 using modulation transfer (MTF)-based filters. The downsampled PAN and MS are treated as the training PAN and training MS images; 2) Regard the original MS image as the ground-truth image (i.e., HRMS); and then 3) Upsample the training MS image by interpolating (polynomial kernel) with 23 coefficients [67] and treating it as LrMS image. When dealing with the full datasets, the original MS images are considered as MS and the upsampled MS images are treated as LrMS, the original PAN images are seen as PAN.

For **hyperspectral dataset**, we choose CAVE indoor dataset to further evaluate our DDRF. The CAVE dataset contains 32 hyperspectral images (HSIs) and corresponding multispectral images (MSIs) with a size of $512 \times 512 \times 31$. 20 images are selected for training and validation, and 11 images remained for testing.

3) *Data Simulation*: For pansharpening datasets, we directly crop the MS image, LrMS image, HRMS image, and PAN image into patches. The train/validation/test split for WV3, GF2, and QB reduced datasets is 9714/1080/20, 19809/2201/20, and 17139/1905/20, respectively. The resolutions of the reduced training dataset are 64×64 for LrMS, PAN, and GT, and 16×16 for MS, respectively. The resolutions of the reduced test dataset are 256×256 for LrMS, PAN and GT, 64×64 for MS, respectively. As for the full-resolution dataset, only test set is needed. The resolution is 512 for LrMS, PAN, and GT, and 128 for MS.

For the hyperspectral dataset, we crop 20 selected images into 3920 overlapping patches for training, where the sizes of HSI and MSI are $16 \times 16 \times 31$ and $64 \times 64 \times 3$, respectively.

B. Benchmark

To assess the performance of our DDRF, we compare it with various state-of-the-art methods of pansharpening (on WV3, GF2, and QB datasets) and additional MHIF (on CAVE dataset).

Specifically, on pansharpening task, we choose some conventional methods containing optimized Brovey transform with haze correction method (BT-H) [68], band-dependent spatial-detail with physical constraints approach (BDS-PC) [69], generalized laplacian pyramid (GLP) with MTF-matched filters with a full scale (FS) regression-based injection model (MTF-GLP-FS) [70] and a set of some competitive deep learning methods including PNN [29], PanNet [31], DiCNN [32], MSDCNN [71], FusionNet [26], LAGNet [33] and DCFNet [72].

On the hyperspectral image fusion task, we also choose conventional and deep learning methods for comparisons, where conventional methods including the coupled sparse tensor factorization (CSTF) method [73], the fast fusion of multi-band images based on solving a Sylvester equation approach (FUSE) [74], the modulation transfer function matched generalized laplacian pyramid hyper-sharpening (MTF-GLP-HS) [70], iterative regularization method based on tensor subspace representation method (IR-TenSR) [75], low tensor-train rank-based (LTTR) method [76] and subspace-based low tensor multi-rank regularization method (LTMR) [77]. For deep learning methods, we perform a comparison with SSRNet [78], ResTFNet [79], FusFormer [80], HSRNet [81] and recent state-of-the-art DHIF [82] method. All deep learning methods are trained with the sample input pairs and converged for fair comparisons.

C. Quality Metric

For the reduced data in pansharpening tasks, we use spectral angle mapper (SAM) [83], the relative dimensionless global error in synthesis (ERGAS) [84], the universal image quality index (Q2ⁿ) [85], and the spatial correlation coefficient (SCC) [86] as fusion metrics. The ideal values for Q2ⁿ and SCC are 1, and for SAM and ERGAS are 0 instead. The metric SAM and ERGAS are defined as Eq. 17 and Eq. 18. Since these metrics require ground truth, they are considered reference metrics. For the full data, since there is no ground truth available, we use non-reference metrics to validate the accuracy of our DDRF. These metrics include D_λ , D_s , and QNR [87]. The QNR has an ideal value of 1 but D_λ , D_s has ideal values of 0.

For hyperspectral data, we additionally use two metrics for evaluation, which are peak signal-to-noise ratio (PSNR) and structural similarity index measure (SSIM) [88]. The optimal values for PSNR and SSIM are $+\infty$ and 1. The metric PSNR is defined as Eq. 19.

$$\text{SAM}(\mathbf{x}, \hat{\mathbf{x}}) = \frac{1}{HW} \sum_{i=1}^{HW} \cos^{-1} \left(\frac{\mathbf{x}_i^\top \hat{\mathbf{x}}_i}{\|\mathbf{x}_i\|_2 \|\hat{\mathbf{x}}_i\|_2} \right), \quad (17)$$

$$\text{ERGAS}(\mathbf{x}, \hat{\mathbf{x}}) = \frac{100}{c} \sqrt{\frac{1}{C} \sum_{i=1}^C \frac{\text{MSE}(\mathbf{x}^i, \hat{\mathbf{x}}^i)}{\mu_{\hat{\mathbf{x}}^i}^2}}, \quad (18)$$

$$\begin{aligned} \text{PSNR}(\mathbf{x}, \hat{\mathbf{x}}) &= \frac{1}{C} \sum_{i=1}^C \text{PSNR}(\mathbf{x}^i, \hat{\mathbf{x}}^i) \\ &= 20 \cdot \log_{10} \left(\frac{\max(\mathbf{x}^i)}{\sqrt{\text{MSE}(\mathbf{x}^i, \hat{\mathbf{x}}^i)}} \right). \end{aligned} \quad (19)$$

D. Results on World-View3 Dataset

We conducted experiments to evaluate our DDRF on the World-View3 dataset and test performances on 20 testing images. We compared our method with three traditional methods and some competitive deep learning methods. The reduced assessments and full assessments are shown in Table. I To clearly demonstrate the advantages of our method, we compare it with other deep learning methods in Figure 4 and zoom in on a certain position to better show the details. Additionally, the error map obtained by comparing it with the GT is also shown.

It can be seen that the deep learning methods have significantly better performances over the traditional methods on average metrics. Among the deep learning methods, our method achieves the best performance on the reduced dataset and competitive performance on the full dataset. Our DDRF can reach 2.77 SAM and 2.05 ERGAS metrics on the reduced dataset, which outperforms all previous deep learning methods. The error map also indicates that the image sampled by DDRF is closer to the GT (with deeper color). The full resolution image sampling by DDRF on the WV3 full dataset has similar image quality to the images fused by other non-generative methods, without color shift and spatial or spectral distortion, which indicates that our DDRF is competitive.

E. Results on GaoFen2 Dataset

We test our DDRF on 20 test images of Gao-Fen2 dataset. As shown in Table. II, our DDRF outperforms previous methods in nearly all reference and non-reference metrics on reduced and full datasets, achieving state-of-the-art performance. Specifically, we observed an improvement of $\approx 18\%/17\%/0.5\%$ in SAM/ERGAS/Q4 metrics when compared with the second best method, i.e., LAGNet [33]. Compared with the third best method, i.e., DCFNet [72], our DDRF improves $\approx 28\%/29\%/1.3\%$ in SAM/ERGAS/Q4 metrics. The state-of-the-art performance in the non-reference metrics on the full dataset reflects that our DDRF can also achieve good results on full-resolution images while only training on small patches. Fig. 5 shows the related close-ups in the rectangular boxes and error maps among the compared deep learning methods. The colors and edge details of object in the figure are closer to the GT. Moreover, the error maps illustrate the residual between the outcome of DDRF and the GT is visually minimal since the overall pseudo-color is the darkest.

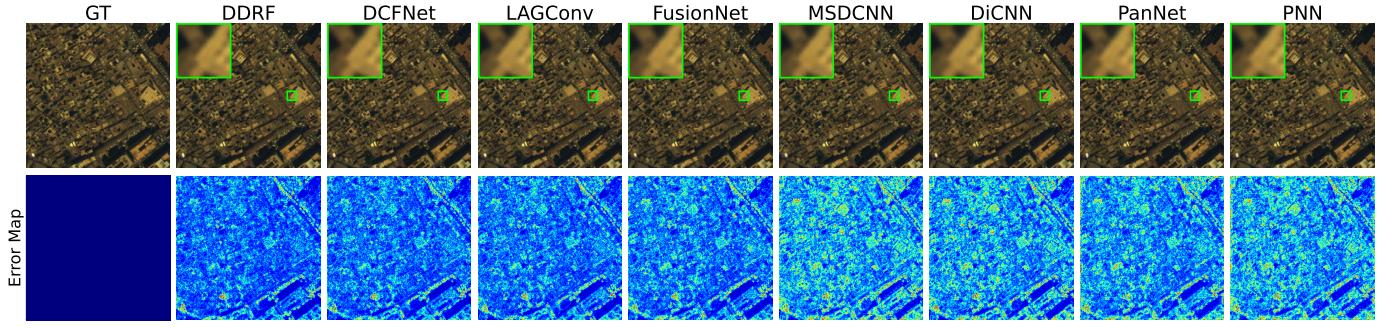


Fig. 4. Visual comparisons with previous pansharpening methods on World-View3 dataset. The first row shows the results by using the pseudo-color. The second row shows the error maps between the GT and fused images. Some close-ups are depicted in green rectangles. Deeper color in the error map means better performance.

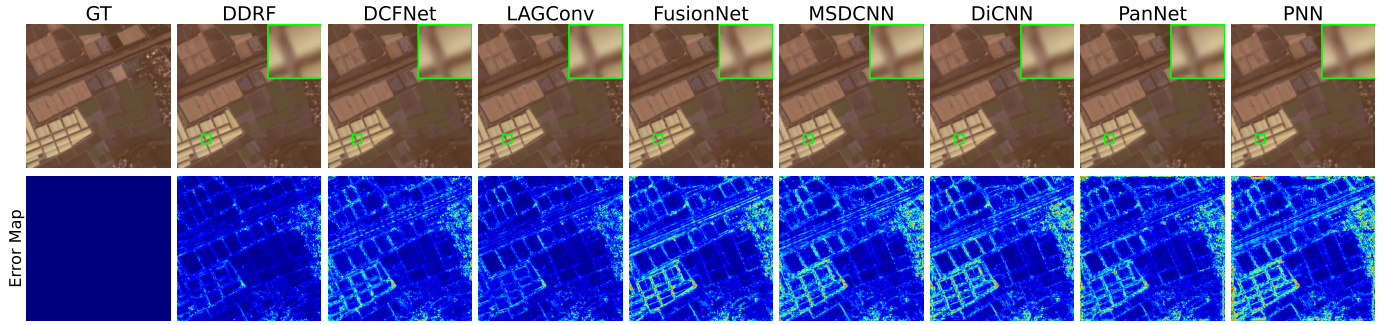


Fig. 5. Visual comparisons with previous pansharpening methods on Gao-Fen2 dataset. The first row shows the results by using the pseudo-color. The second row shows the error maps between the GT and fused images. Some close-ups are depicted in green rectangles. Deeper color in the error map means better performance.

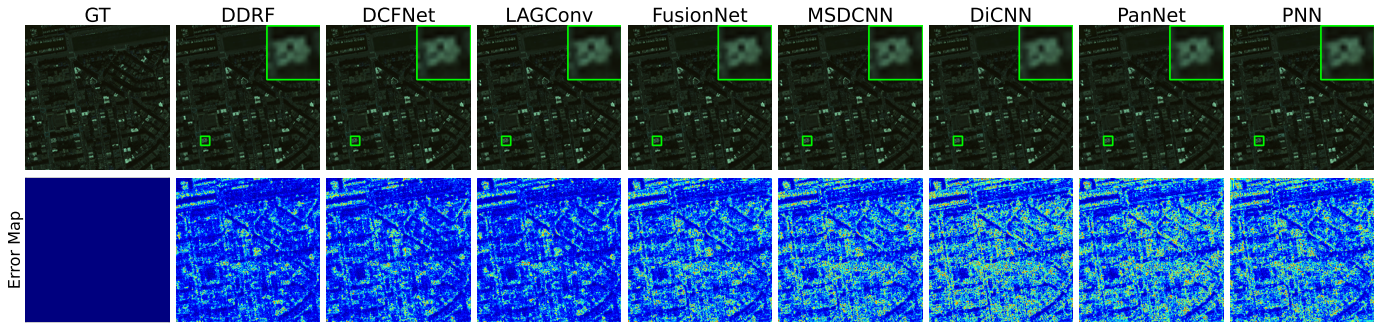


Fig. 6. Visual comparisons with previous pansharpening methods on Quick-Bird dataset. The first row shows the results by using the pseudo-color. The second row shows the error maps between the GT and fused images. Some close-ups are depicted in green rectangles. Deeper color in the error map means better performance.

F. Results on QuickBird Dataset

We also conduct experiments on the QB dataset and assess the reduced and full performances of DDRF. Similarly, the reference and non-reference metrics are obtained on 20 testing images, randomly selected from QB dataset. Performances comparisons are reported in Table. III.

G. Generalization Ability on World-View2 Dataset

Due to the powerful fitting ability of neural networks, they often perform well on data in the same domain. However, once the test data is shifted to a domain that the network has not seen during the training process, the network usually performs poorly. To test the generalization ability of the network, we

evaluated our DDRF model trained on the WV3 dataset to test on the WV2 dataset in a zero-shot manner. Since the imaging parameters of WV2 are similar to WV3, testing on the WV2 dataset can better demonstrate the generalization performance. We also compared our method with other deep learning methods as shown in Table. IV. Our method also achieves competitive results, which demonstrates the good generalization of the diffusion model. This is consistent with some works that apply the diffusion model in a zero-shot manner to tasks such as image generation [60], image classification [89], semantic segmentation [90], and so on.

TABLE I

RESULT OF QUANTITATIVE METRICS ON WV3 REDUCED AND FULL DATASET. SOME CONVENTIONAL METHODS(THE FIRST 3 ROWS), AND DL-BASED METHODS ARE COMPARED. THE BEST RESULTS ARE IN BOLDFACE AND THE SECOND RESULTS ARE IN UNDERLINING.

method	SAM(\pm std)	Reduced ERGAS(\pm std)	Q4(\pm std)	SCC(\pm std)	D_λ (\pm std)	Full D_s (\pm std)	QNR(\pm std)
BDSD-PC	5.4675 \pm 1.7185	4.6549 \pm 1.4667	0.8117 \pm 0.1063	0.9049 \pm 0.0419	0.0625 \pm 0.0235	0.0730 \pm 0.0356	0.8698 \pm 0.0531
MTF-GLP-FS	5.3233 \pm 1.6548	4.6452 \pm 1.4441	0.8177 \pm 0.1014	0.8984 \pm 0.0466	0.0206 \pm 0.0082	0.0630 \pm 0.0284	0.9180 \pm 0.0346
BT-H	4.8985 \pm 1.3028	4.5150 \pm 1.3315	0.8182 \pm 0.1019	0.9240 \pm 0.0243	0.0574 \pm 0.0232	0.0810 \pm 0.0374	0.8670 \pm 0.0540
PNN	3.6798 \pm 0.7625	2.6819 \pm 0.6475	0.8929 \pm 0.0923	0.9761 \pm 0.0075	<u>0.0213\pm0.0080</u>	0.0428 \pm 0.0147	0.9369 \pm 0.0212
PanNet	3.6156 \pm 0.7665	2.6660 \pm 0.6887	0.8906 \pm 0.0934	0.9757 \pm 0.0088	0.0165\pm0.0074	0.0470 \pm 0.0213	<u>0.9374\pm0.0271</u>
DiCNN	3.5929 \pm 0.7623	2.6733 \pm 0.6627	0.9004 \pm 0.0871	0.9763 \pm 0.0072	0.0362 \pm 0.0111	0.0462 \pm 0.0175	0.9195 \pm 0.0258
MSDCNN	3.7773 \pm 0.8032	2.7608 \pm 0.6884	0.8900 \pm 0.0900	0.9741 \pm 0.0076	0.0230 \pm 0.0091	0.0467 \pm 0.0199	0.9316 \pm 0.0271
FusionNet	3.3252 \pm 0.6978	2.4666 \pm 0.6446	0.9044 \pm 0.0904	0.9807 \pm 0.0069	0.0239 \pm 0.0090	0.0364\pm0.0137	0.9406\pm0.0197
LAGNet	3.1042 \pm 0.5585	2.2999 \pm 0.6128	0.9098 \pm 0.0907	0.9838 \pm 0.0068	0.0368 \pm 0.0148	<u>0.0418\pm0.0152</u>	0.9230 \pm 0.0247
DCFNet	<u>3.0264\pm0.7397</u>	<u>2.1588\pm0.4563</u>	<u>0.9051\pm0.0881</u>	<u>0.9861\pm0.0038</u>	0.0781 \pm 0.0812	0.0508 \pm 0.0342	0.8771 \pm 0.1005
DDRF(ours)	2.7722\pm0.5112	2.0484\pm0.4500	0.9191\pm0.0824	0.9877\pm0.0033	0.0741 \pm 0.0628	0.0586 \pm 0.0282	0.8715 \pm 0.0630
Ideal value	0	0	1	1	0	0	1

TABLE II

RESULT OF QUANTITATIVE METRICS ON GF2 REDUCED AND FULL DATASET. SOME CONVENTIONAL METHODS(THE FIRST 3 ROWS), AND DL-BASED METHODS ARE COMPARED. THE BEST RESULTS ARE IN BOLDFACE AND THE SECOND RESULTS ARE IN UNDERLINING.

method	SAM(\pm std)	Reduced ERGAS(\pm std)	Q4(\pm std)	SCC(\pm std)	D_λ (\pm std)	Full D_s (\pm std)	QNR(\pm std)
BDSD-PC	1.7110 \pm 0.3210	1.7025 \pm 0.4056	0.9932 \pm 0.0308	0.9448 \pm 0.0166	0.0759 \pm 0.0301	0.1548 \pm 0.0280	0.7812 \pm 0.0409
MTF-GLP-FS	1.6757 \pm 0.3457	1.6023 \pm 0.3545	0.8914 \pm 0.0256	0.9390 \pm 0.0197	0.0759 \pm 0.0301	0.1548 \pm 0.0280	0.7812 \pm 0.0409
BT-H	1.6810 \pm 0.3168	1.5524 \pm 0.3642	0.9089 \pm 0.0292	0.9508 \pm 0.0150	0.0602 \pm 0.0252	0.1313 \pm 0.0193	0.8165 \pm 0.0305
PNN	1.0477 \pm 0.2264	1.0572 \pm 0.2355	0.9604 \pm 0.0100	0.9772 \pm 0.0054	0.0367 \pm 0.0291	0.0943 \pm 0.0224	0.8726 \pm 0.0373
PanNet	0.9967 \pm 0.2119	0.9192 \pm 0.1906	0.9671 \pm 0.0099	0.9829 \pm 0.0035	<u>0.0206\pm0.0112</u>	0.0799 \pm 0.0178	0.9011 \pm 0.0203
DiCNN	1.0525 \pm 0.2310	1.0812 \pm 0.2510	0.9594 \pm 0.0101	0.9771 \pm 0.0058	0.0413 \pm 0.0128	0.0992 \pm 0.0131	0.8636 \pm 0.0165
MSDCNN	1.0472 \pm 0.2210	1.0413 \pm 0.2309	0.9612 \pm 0.0108	0.9782 \pm 0.0050	0.0269 \pm 0.0131	0.0730 \pm 0.0093	0.9020 \pm 0.0128
FusionNet	0.9735 \pm 0.2117	0.9878 \pm 0.2222	0.9641 \pm 0.0093	0.9806 \pm 0.0049	0.0400 \pm 0.0126	0.1013 \pm 0.0134	0.8628 \pm 0.0184
LAGNet	<u>0.7859\pm0.1478</u>	<u>0.6869\pm0.1125</u>	<u>0.9804\pm0.0085</u>	0.9906\pm0.0019	0.0324 \pm 0.0130	0.0792 \pm 0.0136	0.8910 \pm 0.0204
DCFNet	0.8896 \pm 0.1577	0.8061 \pm 0.1369	0.9727 \pm 0.0100	0.9853 \pm 0.0024	0.0234 \pm 0.0116	<u>0.0659\pm0.0096</u>	<u>0.9122\pm0.0119</u>
DDRF(ours)	0.6408\pm0.1203	0.5668\pm0.1010	0.9855\pm0.0078	<u>0.9859\pm0.0035</u>	0.0201\pm0.0109	0.0408\pm0.0103	0.9398\pm0.0137
Ideal value	0	0	1	1	0	0	1

TABLE III

RESULT OF QUANTITATIVE METRICS ON QB REDUCED AND FULL DATASET. SOME CONVENTIONAL METHODS(THE FIRST 3 ROWS), AND DL-BASED METHODS ARE COMPARED. THE BEST RESULTS ARE IN BOLDFACE AND THE SECOND RESULTS ARE IN UNDERLINING.

method	SAM(\pm std)	Reduced ERGAS(\pm std)	Q4(\pm std)	SCC(\pm std)	D_λ (\pm std)	Full D_s (\pm std)	QNR(\pm std)
BDSD-PC	8.2620 \pm 2.0497	7.5420 \pm 0.8138	0.8323 \pm 0.1013	0.9030 \pm 0.0181	0.1975 \pm 0.0334	0.1636 \pm 0.0483	0.6722 \pm 0.0577
MTF-GLP-FS	8.1131 \pm 1.9553	7.5102 \pm 0.7926	0.8296 \pm 0.0905	0.8998 \pm 0.0196	0.0489 \pm 0.0149	0.1383 \pm 0.0238	0.8199 \pm 0.0340
BT-H	7.1943 \pm 1.5523	7.4008 \pm 0.8378	0.8326 \pm 0.0880	0.9156 \pm 0.0152	0.2300 \pm 0.0718	0.1648 \pm 0.0167	0.6434 \pm 0.0645
PNN	5.2054 \pm 0.9625	4.4722 \pm 0.3734	0.9180 \pm 0.0938	0.9711 \pm 0.0123	0.0569 \pm 0.0112	0.0624 \pm 0.0239	<u>0.8844\pm0.0304</u>
PanNet	5.7909 \pm 1.1839	5.8629 \pm 0.8883	0.8850 \pm 0.0917	0.9485 \pm 0.0170	0.0410\pm0.0108	0.1137 \pm 0.0323	0.8502 \pm 0.0390
DiCNN	5.3795 \pm 1.0266	5.1354 \pm 0.4876	0.9042 \pm 0.0942	0.9621 \pm 0.0133	0.0920 \pm 0.0143	0.1067 \pm 0.0210	0.8114 \pm 0.0310
FusionNet	4.9226 \pm 0.9077	4.1594 \pm 0.3212	0.9252 \pm 0.0902	0.9755 \pm 0.0104	0.0586 \pm 0.0189	0.0522\pm0.0088	0.8922\pm0.0219
LAGNet	4.5473 \pm 0.8296	<u>3.8259\pm0.4196</u>	<u>0.9335\pm0.0878</u>	<u>0.9807\pm0.0091</u>	0.0844 \pm 0.0238	0.0676 \pm 0.0136	0.8536 \pm 0.0178
DCFNet	<u>4.5383\pm0.7397</u>	3.8315 \pm 0.2915	0.9325 \pm 0.0903	0.9741 \pm 0.0101	<u>0.0454\pm0.0147</u>	0.1239 \pm 0.0269	0.8360 \pm 0.0158
DDRF(ours)	4.3529\pm0.7319	3.5659\pm0.2845	0.9380\pm0.0896	0.9838\pm0.0073	0.1025 \pm 0.0266	<u>0.0552\pm0.0228</u>	0.8484 \pm 0.0416
Ideal value	0	0	1	1	0	0	1

H. Additional Experiments on Hyperspectral Dataset

We additionally conducted experiments on the hyperspectral CAVE dataset, and the results and comparisons with other methods can be found in Table V. Note that compared to the state-of-the-art hyperspectral fusion method DHIF [82], our method achieves a 0.1dB higher PSNR and a higher Q2n,

as well as competitive performance in other metrics. Fusion images and error maps are similarly plotted as shown in Fig. 8. To directly illustrate the spectral accuracy, the spectral responses of pixels in two testing images are compared and shown in Fig. IV-H, which shows that our DDRF has a more accurate spectral response.

TABLE IV

GENERALIZATION ABILITY OF DL-BASED METHODS ARE COMPARED. THE BEST RESULTS ARE IN BOLDFACE AND THE SECOND RESULTS ARE IN UNDERLINING.

method	Reduced				Full		
	SAM(\pm std)	ERGAS(\pm std)	Q4(\pm std)	SCC(\pm std)	D_λ (\pm std)	D_s (\pm std)	QNR(\pm std)
PNN	7.1158 \pm 1.6812	5.6152 \pm 0.9431	0.7619 \pm 0.0928	0.8782 \pm 0.0175	0.1484 \pm 0.0957	0.0771 \pm 0.0169	0.7869 \pm 0.0959
PanNet	<u>5.4948\pm0.7126</u>	4.3371\pm0.5197	0.8401\pm0.0796	0.9177\pm0.0081	<u>0.0317\pm0.0173</u>	0.0191\pm0.0123	0.9500\pm0.0275
DiCNN	6.9216 \pm 0.7898	6.2507 \pm 0.5745	0.7205 \pm 0.0746	0.8552 \pm 0.0289	0.1412 \pm 0.0661	0.1023 \pm 0.0195	0.7700 \pm 0.0505
MSDCNN	6.0064 \pm 0.6377	4.7438 \pm 0.4939	0.8241 \pm 0.0799	0.8972 \pm 0.0109	0.0589 \pm 0.0421	0.0290 \pm 0.0138	0.9143 \pm 0.0516
FusionNet	6.4257 \pm 0.8602	5.1363 \pm 0.5151	0.7961 \pm 0.0737	0.8746 \pm 0.0134	0.0519 \pm 0.0292	0.0559 \pm 0.0146	0.8948 \pm 0.0187
LAGNet	6.9545 \pm 0.4739	5.3262 \pm 0.3185	0.8054 \pm 0.0837	0.9125 \pm 0.0101	0.1302 \pm 0.0856	0.0547 \pm 0.0159	0.8229 \pm 0.0884
DCFNet	5.6194 \pm 0.6039	<u>4.4887\pm0.3764</u>	<u>0.8292\pm0.0815</u>	<u>0.9154\pm0.0083</u>	0.0649 \pm 0.0357	0.0700 \pm 0.0219	0.8690 \pm 0.0233
DDRF(ours)	5.3827\pm0.5737	4.6712 \pm 0.4155	0.8217 \pm 0.0777	0.8993 \pm 0.0129	0.0313\pm0.0376	<u>0.0312\pm0.0111</u>	<u>0.9388\pm0.0453</u>
Ideal value	0	0	1	1	0	0	1

TABLE V

RESULT OF QUANTITATIVE METRICS ON CAVE $\times 4$ HYPERSPECTRAL DATASET. SOME CONVENTIONAL METHODS AND DEEP LEARNING METHODS ARE COMPARED. THE BOLD NUMBER NOTES THE BEST RESULT AND THE UNDERLINED NUMBER MEANS THE SECOND-BEST RESULT.

method	PSNR(\pm std)	SSIM(\pm std)	Q2n(\pm std)	SAM(\pm std)	ERGAS(\pm std)
FUSE	17.7748 \pm 4.5346	0.3942 \pm 0.1710	0.0892 \pm 0.0535	34.2973 \pm 6.4079	37.9144 \pm 7.0933
CSTF-FUS	34.4632 \pm 4.2806	0.8662 \pm 0.0747	0.6659 \pm 0.1586	14.3683 \pm 5.3020	8.2885 \pm 5.2848
IR-TenSR	35.6081 \pm 3.4461	0.9451 \pm 0.0267	0.7774 \pm 0.1228	12.2950 \pm 4.6825	5.8969 \pm 3.0455
LTTR	35.8505 \pm 3.4883	0.9562 \pm 0.0288	0.8404 \pm 0.0979	6.9895 \pm 2.5542	5.9904 \pm 2.9211
LTMR	36.5434 \pm 3.2995	0.9631 \pm 0.0208	0.8416 \pm 0.1031	6.7105 \pm 2.1934	5.3868 \pm 2.5286
MTF-GLP-HS	37.6920 \pm 3.8528	0.9725 \pm 0.0158	0.8716 \pm 0.0847	5.3281 \pm 1.9119	4.5749 \pm 2.6605
UTV	38.6153 \pm 4.0640	0.9410 \pm 0.0434	0.7752 \pm 0.1416	8.6488 \pm 3.3764	4.5189 \pm 2.8173
ResTFNet	45.5842 \pm 5.4647	0.9939 \pm 0.0055	0.9581 \pm 0.0315	2.7643 \pm 0.6988	2.3134 \pm 2.4377
SSRNet	48.6196 \pm 3.9182	0.9954 \pm 0.0024	0.9598 \pm 0.0309	2.5415 \pm 0.8369	1.6358 \pm 1.2191
Fusformer	49.9831 \pm 8.0965	0.9943 \pm 0.0114	0.9624 \pm 0.0362	2.2033 \pm 0.8510	2.5337 \pm 5.3052
HSRNet	50.3805 \pm 3.3802	0.9970 \pm 0.0015	0.9666 \pm 0.0290	2.2272 \pm 0.6575	1.2002\pm0.7506
DHIF	<u>51.0721\pm4.1648</u>	0.9973\pm0.0017	0.9695 \pm 0.0267	2.0080\pm0.6304	<u>1.2216\pm0.9653</u>
DDRF(ours)	51.1758\pm4.6148	<u>0.9971\pm0.0026</u>	0.9737\pm0.0106	<u>2.0952\pm0.6471</u>	1.2996 \pm 1.2822
Ideal value	∞	1	1	0	0

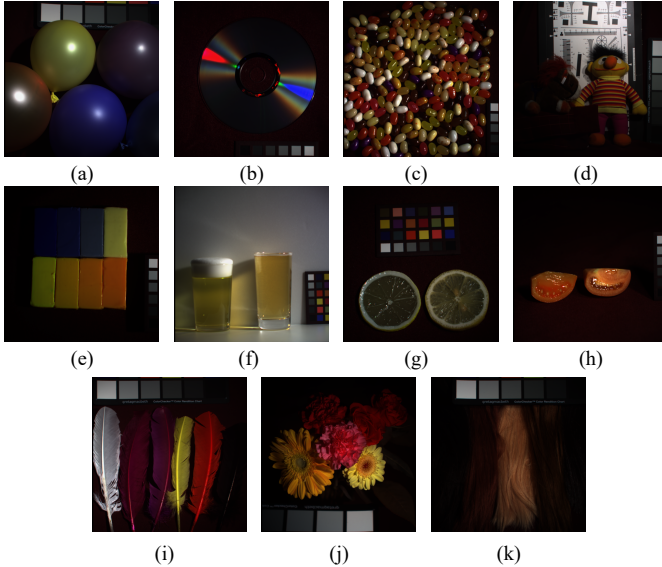


Fig. 7. Testing images from the CAVE dataset. (a) Balloons. (b) Compact disc (CD). (c) Jelly beans. (d) Chart and stuffed toy. (e) Clay. (f) Fake and real beers. (g) Fake and real lemon slices. (h) Fake and real tomatoes. (i) Feathers. (j) Flowers. (k) Hairs. An RGB color representation is used to depict the images.

I. Ablation Study

We conduct an ablation study on proposed modules and techniques to verify their effectiveness.

1) *Condition Injection*: We propose two condition injection modules called style transfer modulation and wavelet modulation which are respectively responsible for coarse-grain overall style condition injection and fine-grain detail condition injection. Without using them, one direct way to inject condition information is concatenating condition and noisy input along the channel dimension. We ablate these two different techniques by training the diffusion model with the following forms,

- only concatenating condition and input together,
- only using coarse-grain style transfer modulation,
- conducting two modulations in the diffusion model.

Each of these trained models is converged for a fair comparison. The performances on WV3 reduced dataset are reported in Table. VI. With the addition of style modulation and wavelet modulation, the performance of fusion exhibits a monotonically increasing trend. It should be noted that without these two modulations, DDRF will degrade to DDPM with residual learning, indicating that directly applying DDPM to the fusion task performs poorly.

2) *Residual Learning*: To verify the effectiveness of residual learning, we return the input to the noisy HRMS as

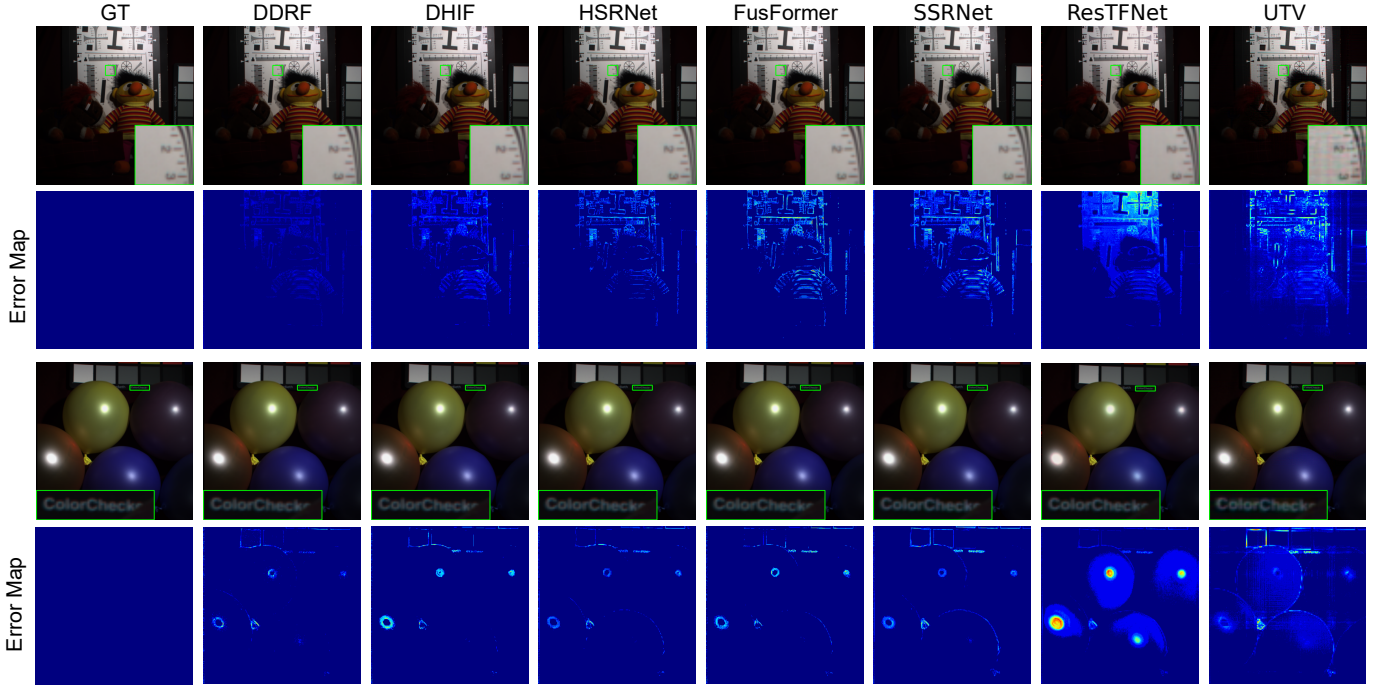


Fig. 8. The first and third rows shows the results by using RGB color on "chart and stuffed toy" and "ballons", respectively. Some details are depicted in the green rectangles and zoomed in. The second and fourth rows show the error maps between the GT and the fused images using pseudo-color. The darker error maps indicate better performances.

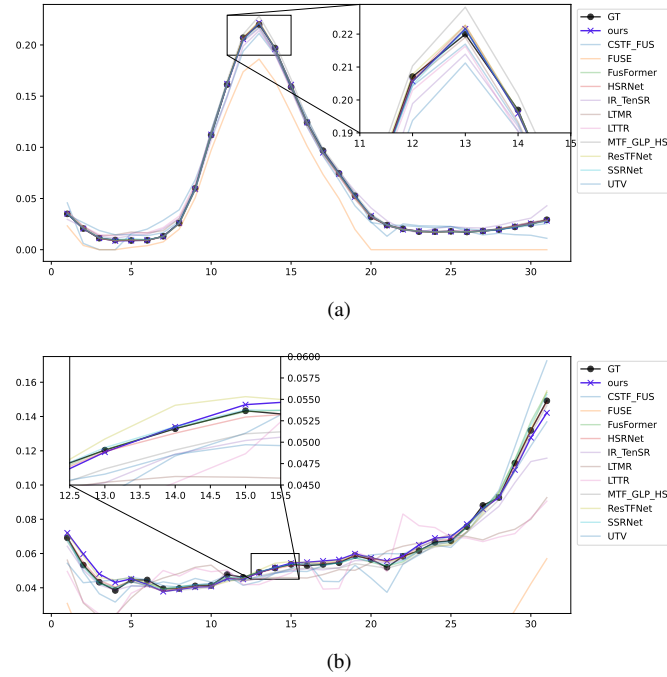


Fig. 9. Spectral vectors of the GT, our DDRF and benchmarks. (a) Spectral vectors in "feather" located at position (380, 200). (b) Spectral vectors in "chart and stuffed toy" located at position (200, 200). The horizontal axis represents the band number and the vertical axis represents pixel values.

TABLE VI
ABLATION ON TWO MODULATION MODULES.

Style Transfer Modulation	Wavelet Modulation	SAM(\pm std)	ERGAS(\pm std)	Q8(\pm std)	SCC(\pm std)
✓		3.2851 \pm 0.6828	2.5501 \pm 0.6141	0.8981 \pm 0.0904	0.9796 \pm 0.0067
	✓	3.1418 \pm 0.5789	2.3527 \pm 0.5116	0.8971 \pm 0.0940	0.9837 \pm 0.0047
✓	✓	2.7722\pm0.5112	2.0484\pm0.4500	0.9191\pm0.0824	0.9877\pm0.0033

\mathbf{x}_t . Then we retrain the diffusion model until the model is converged and gain its performance on WV3 dataset as shown in Table. VII. With residual learning, the diffusion model can output fused images closer to the GT. One hypothesis is that the residual distribution is "simpler" than the HRMS distribution, which benefits the model to learn more efficiently. A direct way to express the complexity of a distribution is to the entropy. We computed the pixel entropy of the HRMS and residual image (i.e., HRMS - LrMS) and found that the entropy of HRMS is 6.498 bits-per-pixel (bpp) but the residual image is only 4.461 bpp, which indicates the distribution of the residual image is simpler.

TABLE VII
ABLATION ON USING RESIDUAL LEARNING.

Residual Learning	SAM(\pm std)	ERGAS(\pm std)	Q8(\pm std)	SCC(\pm std)
✓	3.2397 \pm 0.4546	3.2096 \pm 1.003	0.9061 \pm 0.0837	0.9729 \pm 0.0113
	2.7722\pm0.5112	2.0484\pm0.4500	0.9191\pm0.0824	0.9877\pm0.0033

3) *Prediction Objective*: The prediction objective of the model can be ϵ , \mathbf{x}_0 , or \mathbf{v} . ϵ means that the model needs to predict the added Gaussian noise, \mathbf{x}_0 indicates the model predicts the original clean image from the noisy image, and \mathbf{v}

reflects that model predicts the weighted sum of noise and \mathbf{x}_0 . We changed the training objectives of the network to these three types separately and trained the diffusion model to convergency on the WV3 dataset. Their performances are shown in Table. VIII. As can be seen that predicting \mathbf{x}_0 performs the best. We suppose that for the small-scale datasets, \mathbf{x}_0 is more straightforward than ϵ and \mathbf{v} since the sample density is more concentrated, but as for large-scale datasets, predicting ϵ and \mathbf{v} can force the network to learn detailed denoising trajectory which is useful to generate images with high-level conditions, such as classification label [91], text [37] and bounding box [92].

TABLE VIII
ABLATION ON TRAINING OBJECTIVES OF THE DIFFUSION MODEL.

Objective	SAM(\pm std)	ERGAS(\pm std)	Q8(\pm std)	SCC(\pm std)
ϵ	3.7702 \pm 0.6397	2.7954 \pm 0.6516	0.8388 \pm 0.1181	0.9794 \pm 0.0064
\mathbf{v}	3.4853 \pm 0.6080	2.6624 \pm 0.5912	0.8715 \pm 0.1025	0.9808 \pm 0.0052
\mathbf{x}_0	2.7722\pm0.5112	2.0484\pm0.4500	0.9191\pm0.0824	0.9877\pm0.0033

V. CONCLUSIONS

In this paper, we proposed a denoising diffusion model named DDRF for remote sensing image fusion tasks. To make DDRF suit the fusion task, we design two novel feature modulation modules: the style modulation module and wavelet modulation module responsible for coarse-grained style information modulation and fine-grained details modulation, respectively. We also discussed residual learning and some choices of training objectives. Experiments conducted on commonly used satellite datasets and an additional hyperspectral dataset demonstrated our DDRF can outperform previous image fusion methods. Our method first introduces the denoising diffusion model into the remote sensing fusion, we hope our work can inspire later works for better applying the diffusion model for the remote sensing fusion field.

REFERENCES

- [1] C. Wu, B. Du, X. Cui, and L. Zhang, "A post-classification change detection method based on iterative slow feature analysis and bayesian soft fusion," *Remote Sensing of Environment*, vol. 199, pp. 241–255, 2017.
- [2] W. G. C. Bandara, N. G. Nair, and V. M. Patel, "Ddpm-cd: Remote sensing change detection using denoising diffusion probabilistic models," *arXiv preprint arXiv:2206.11892*, 2022.
- [3] C. A. Bishop, J. G. Liu, and P. J. Mason, "Hyperspectral remote sensing for mineral exploration in pulang, yunnan province, china," *International Journal of Remote Sensing*, vol. 32, no. 9, pp. 2409–2426, 2011.
- [4] T. A. Carrino, A. P. Crósta, C. L. B. Toledo, and A. M. Silva, "Hyperspectral remote sensing applied to mineral exploration in southern peru: A multiple data integration approach in the chapí chiara gold prospect," *International journal of applied earth observation and geoinformation*, vol. 64, pp. 287–300, 2018.
- [5] M. D. Hossain and D. Chen, "Segmentation for object-based image analysis (obia): A review of algorithms and challenges from remote sensing perspective," *ISPRS Journal of Photogrammetry and Remote Sensing*, vol. 150, pp. 115–134, 2019.
- [6] P. Kwarteng and A. Chavez, "Extracting spectral contrast in landsat thematic mapper image data using selective principal component analysis," *Photogramm. Eng. Remote Sens.*, vol. 55, no. 1, pp. 339–348, 1989.
- [7] C. A. Laben and B. V. Brower, "Process for enhancing the spatial resolution of multispectral imagery using pan-sharpening," Jan. 4 2000, uS Patent 6,011,875.

- [8] B. Aiazzi, S. Baronti, and M. Selva, "Improving component substitution pansharpening through multivariate regression of ms + pan data," *IEEE Transactions on Geoscience and Remote Sensing*, vol. 45, no. 10, pp. 3230–3239, 2007.
- [9] J. Qu, Y. Li, and W. Dong, "Hyperspectral pansharpening with guided filter," *IEEE Geoscience and Remote Sensing Letters*, vol. 14, no. 11, pp. 2152–2156, 2017.
- [10] X. Otazu, M. González-Audifána, O. Fors, and J. Núñez, "Introduction of sensor spectral response into image fusion methods. application to wavelet-based methods," *IEEE Transactions on Geoscience and Remote Sensing*, vol. 43, no. 10, pp. 2376–2385, 2005.
- [11] J. Liu, "Smoothing filter-based intensity modulation: A spectral preserve image fusion technique for improving spatial details," *International Journal of remote sensing*, vol. 21, no. 18, pp. 3461–3472, 2000.
- [12] B. Aiazzi, L. Alparone, S. Baronti, A. Garzelli, and M. Selva, "Mtf-tailored multiscale fusion of high-resolution ms and pan imagery," *Photogrammetric Engineering & Remote Sensing*, vol. 72, no. 5, pp. 591–596, 2006.
- [13] G. Vivone, R. Restaino, M. Dalla Mura, G. Licciardi, and J. Chanussot, "Contrast and error-based fusion schemes for multispectral image pansharpening," *IEEE Geoscience and Remote Sensing Letters*, vol. 11, no. 5, pp. 930–934, 2013.
- [14] X. He, L. Condat, J. M. Bioucas-Dias, J. Chanussot, and J. Xia, "A new pansharpening method based on spatial and spectral sparsity priors," *IEEE Transactions on Image Processing*, vol. 23, no. 9, pp. 4160–4174, 2014.
- [15] T. Wang, F. Fang, F. Li, and G. Zhang, "High-quality bayesian pansharpening," *IEEE Transactions on Image Processing*, vol. 28, no. 1, pp. 227–239, 2018.
- [16] M. Moeller, T. Wittman, and A. L. Bertozzi, "A variational approach to hyperspectral image fusion," in *Algorithms and Technologies for Multispectral, Hyperspectral, and Ultraspectral Imagery XV*, vol. 7334. SPIE, 2009, pp. 502–511.
- [17] J. Duran, A. Buades, B. Coll, and C. Sbert, "A nonlocal variational model for pansharpening image fusion," *SIAM Journal on Imaging Sciences*, vol. 7, no. 2, pp. 761–796, 2014.
- [18] T. Xu, T.-Z. Huang, L.-J. Deng, X.-L. Zhao, and J. Huang, "Hyperspectral image superresolution using unidirectional total variation with tucker decomposition," *IEEE Journal of Selected Topics in Applied Earth Observations and Remote Sensing*, vol. 13, pp. 4381–4398, 2020.
- [19] K. He, X. Zhang, S. Ren, and J. Sun, "Deep residual learning for image recognition," in *Proceedings of the IEEE conference on computer vision and pattern recognition*, 2016, pp. 770–778.
- [20] O. Ronneberger, P. Fischer, and T. Brox, "U-net: Convolutional networks for biomedical image segmentation," in *Medical Image Computing and Computer-Assisted Intervention—MICCAI 2015: 18th International Conference, Munich, Germany, October 5–9, 2015, Proceedings, Part III 18*. Springer, 2015, pp. 234–241.
- [21] Z. Liu, Y. Lin, Y. Cao, H. Hu, Y. Wei, Z. Zhang, S. Lin, and B. Guo, "Swin transformer: Hierarchical vision transformer using shifted windows," in *Proceedings of the IEEE/CVF international conference on computer vision*, 2021, pp. 10012–10022.
- [22] W. Wang, E. Xie, X. Li, D.-P. Fan, K. Song, D. Liang, T. Lu, P. Luo, and L. Shao, "Pyramid vision transformer: A versatile backbone for dense prediction without convolutions," in *Proceedings of the IEEE/CVF international conference on computer vision*, 2021, pp. 568–578.
- [23] J. Lehtinen, J. Munkberg, J. Hasselgren, S. Laine, T. Karras, M. Aittala, and T. Aila, "Noise2noise: Learning image restoration without clean data," *arXiv preprint arXiv:1803.04189*, 2018.
- [24] L. Chen, X. Chu, X. Zhang, and J. Sun, "Simple baselines for image restoration," in *Computer Vision—ECCV 2022: 17th European Conference, Tel Aviv, Israel, October 23–27, 2022, Proceedings, Part VII*. Springer, 2022, pp. 17–33.
- [25] X. Chu, L. Chen, and W. Yu, "Nafssr: stereo image super-resolution using nafnet," in *Proceedings of the IEEE/CVF Conference on Computer Vision and Pattern Recognition*, 2022, pp. 1239–1248.
- [26] L.-J. Deng, G. Vivone, C. Jin, and J. Chanussot, "Detail injection-based deep convolutional neural networks for pansharpening," *IEEE Transactions on Geoscience and Remote Sensing*, vol. 59, no. 8, pp. 6995–7010, 2020.
- [27] S.-Q. Deng, L.-J. Deng, X. Wu, R. Ran, D. Hong, and G. Vivone, "Psrt: Pyramid shuffle-and-reshuffle transformer for multispectral and hyperspectral image fusion," *IEEE Transactions on Geoscience and Remote Sensing*, 2023.
- [28] H. Xu, J. Ma, J. Jiang, X. Guo, and H. Ling, "U2fusion: A unified unsupervised image fusion network," *IEEE Transactions on Pattern Analysis and Machine Intelligence*, vol. 44, no. 1, pp. 502–518, 2020.

- [29] G. Masi, D. Cozzolino, L. Verdoliva, and G. Scarpa, "Pansharpening by convolutional neural networks," *Remote Sensing*, vol. 8, no. 7, p. 594, 2016.
- [30] C. Dong, C. C. Loy, K. He, and X. Tang, "Image super-resolution using deep convolutional networks," *IEEE transactions on pattern analysis and machine intelligence*, vol. 38, no. 2, pp. 295–307, 2015.
- [31] J. Yang, X. Fu, Y. Hu, Y. Huang, X. Ding, and J. Paisley, "Pannet: A deep network architecture for pan-sharpening," in *Proceedings of the IEEE international conference on computer vision*, 2017, pp. 5449–5457.
- [32] L. He, Y. Rao, J. Li, J. Chanussot, A. Plaza, J. Zhu, and B. Li, "Pansharpening via detail injection based convolutional neural networks," *IEEE Journal of Selected Topics in Applied Earth Observations and Remote Sensing*, vol. 12, no. 4, pp. 1188–1204, 2019.
- [33] Z.-R. Jin, T.-J. Zhang, T.-X. Jiang, G. Vivone, and L.-J. Deng, "Lagconv: Local-context adaptive convolution kernels with global harmonic bias for pansharpening," in *Proceedings of the AAAI Conference on Artificial Intelligence*, vol. 36, no. 1, 2022, pp. 1113–1121.
- [34] A. Q. Nichol and P. Dhariwal, "Improved denoising diffusion probabilistic models," in *International Conference on Machine Learning*. PMLR, 2021, pp. 8162–8171.
- [35] T. Karras, M. Aittala, T. Aila, and S. Laine, "Elucidating the design space of diffusion-based generative models," *arXiv preprint arXiv:2206.00364*, 2022.
- [36] C. Saharia, W. Chan, S. Saxena, L. Li, J. Whang, E. Denton, S. K. S. Ghasemipour, B. K. Ayan, S. S. Mahdavi, R. G. Lopes *et al.*, "Photorealistic text-to-image diffusion models with deep language understanding," *arXiv preprint arXiv:2205.11487*, 2022.
- [37] R. Rombach, A. Blattmann, D. Lorenz, P. Esser, and B. Ommer, "High-resolution image synthesis with latent diffusion models," in *Proceedings of the IEEE/CVF Conference on Computer Vision and Pattern Recognition*, 2022, pp. 10 684–10 695.
- [38] C. Saharia, W. Chan, H. Chang, C. Lee, J. Ho, T. Salimans, D. Fleet, and M. Norouzi, "Palette: Image-to-image diffusion models," in *ACM SIGGRAPH 2022 Conference Proceedings*, 2022, pp. 1–10.
- [39] X. L. Li, J. Thickstun, I. Gulrajani, P. Liang, and T. B. Hashimoto, "Diffusion-lm improves controllable text generation," *arXiv preprint arXiv:2205.14217*, 2022.
- [40] Y. Song, J. Sohl-Dickstein, D. P. Kingma, A. Kumar, S. Ermon, and B. Poole, "Score-based generative modeling through stochastic differential equations," *arXiv preprint arXiv:2011.13456*, 2020.
- [41] Y. Song and S. Ermon, "Generative modeling by estimating gradients of the data distribution," *Advances in neural information processing systems*, vol. 32, 2019.
- [42] J. Ho and T. Salimans, "Classifier-free diffusion guidance," *arXiv preprint arXiv:2207.12598*, 2022.
- [43] J. Song, C. Meng, and S. Ermon, "Denoising diffusion implicit models," *arXiv preprint arXiv:2010.02502*, 2020.
- [44] C. Lu, Y. Zhou, F. Bao, J. Chen, C. Li, and J. Zhu, "Dpm-solver: A fast ode solver for diffusion probabilistic model sampling in around 10 steps," *arXiv preprint arXiv:2206.00927*, 2022.
- [45] S. Peng, L.-J. Deng, J.-F. Hu, and Y. Zhuo, "Source-adaptive discriminative kernels based network for remote sensing pansharpening," in *Proc. 31st Int. Joint Conf. Artif. Intell.*, 2022.
- [46] Z.-X. Chen, C. Jin, T.-J. Zhang, X. Wu, and L.-J. Deng, "Spanconv: A new convolution via spanning kernel space for lightweight pansharpening," in *Proc. 31st Int. Joint Conf. Artif. Intell.*, 2022, pp. 1–7.
- [47] Y. Liang, P. Zhang, Y. Mei, and T. Wang, "Pmacnet: Parallel multiscale attention constraint network for pan-sharpening," *IEEE Geoscience and Remote Sensing Letters*, vol. 19, pp. 1–5, 2022.
- [48] I. Goodfellow, J. Pouget-Abadie, M. Mirza, B. Xu, D. Warde-Farley, S. Ozair, A. Courville, and Y. Bengio, "Generative adversarial nets," in *Advances in Neural Information Processing Systems*, Z. Ghahramani, M. Welling, C. Cortes, N. Lawrence, and K. Weinberger, Eds., vol. 27. Curran Associates, Inc., 2014.
- [49] M. Arjovsky, S. Chintala, and L. Bottou, "Wasserstein generative adversarial networks," in *International conference on machine learning*. PMLR, 2017, pp. 214–223.
- [50] I. Gulrajani, F. Ahmed, M. Arjovsky, V. Dumoulin, and A. C. Courville, "Improved training of wasserstein gans," *Advances in neural information processing systems*, vol. 30, 2017.
- [51] T. Karras, S. Laine, and T. Aila, "A style-based generator architecture for generative adversarial networks," in *Proceedings of the IEEE/CVF conference on computer vision and pattern recognition*, 2019, pp. 4401–4410.
- [52] T. Karras, S. Laine, M. Aittala, J. Hellsten, J. Lehtinen, and T. Aila, "Analyzing and improving the image quality of StyleGAN," in *Proc. CVPR*, 2020.
- [53] J. Ma, W. Yu, C. Chen, P. Liang, X. Guo, and J. Jiang, "Pan-gan: An unsupervised pan-sharpening method for remote sensing image fusion," *Information Fusion*, vol. 62, pp. 110–120, 2020.
- [54] W. Diao, F. Zhang, J. Sun, Y. Xing, K. Zhang, and L. Bruzzone, "Zer-gan: Zero-reference gan for fusion of multispectral and panchromatic images," *IEEE Transactions on Neural Networks and Learning Systems*, pp. 1–15, 2022.
- [55] L. Dinh, J. Sohl-Dickstein, and S. Bengio, "Density estimation using real nvp," *arXiv preprint arXiv:1605.08803*, 2016.
- [56] D. P. Kingma and P. Dhariwal, "Glow: Generative flow with invertible 1x1 convolutions," *Advances in neural information processing systems*, vol. 31, 2018.
- [57] K. Preechakul, N. Chatthee, S. Wizadwongsa, and S. Suwajanakorn, "Diffusion autoencoders: Toward a meaningful and decodable representation," in *Proceedings of the IEEE/CVF Conference on Computer Vision and Pattern Recognition*, 2022, pp. 10 619–10 629.
- [58] C. Saharia, J. Ho, W. Chan, T. Salimans, D. J. Fleet, and M. Norouzi, "Image super-resolution via iterative refinement," *IEEE Transactions on Pattern Analysis and Machine Intelligence*, 2022.
- [59] B. Kawar, M. Elad, S. Ermon, and J. Song, "Denoising diffusion restoration models," *arXiv preprint arXiv:2201.11793*, 2022.
- [60] Y. Wang, J. Yu, and J. Zhang, "Zero-shot image restoration using denoising diffusion null-space model," *arXiv preprint arXiv:2212.00490*, 2022.
- [61] W. Wang, J. Bao, W. Zhou, D. Chen, D. Chen, L. Yuan, and H. Li, "Sindiffusion: Learning a diffusion model from a single natural image," *arXiv preprint arXiv:2211.12445*, 2022.
- [62] J. Zhang, J. Guo, S. Sun, J.-G. Lou, and D. Zhang, "Layoutdiffusion: Improving graphic layout generation by discrete diffusion probabilistic models," 2023.
- [63] Y. Song and S. Ermon, "Generative modeling by estimating gradients of the data distribution," *Advances in neural information processing systems*, vol. 32, 2019.
- [64] W. G. C. Bandara, N. G. Nair, and V. M. Patel, "Ddpm-cd: Remote sensing change detection using denoising diffusion probabilistic models," *arXiv preprint arXiv:2206.11892*, 2022.
- [65] J. Yue, L. Fang, S. Xia, Y. Deng, and J. Ma, "Dif-fusion: Towards high color fidelity in infrared and visible image fusion with diffusion models," *arXiv preprint arXiv:2301.08072*, 2023.
- [66] L. Wald, T. Ranchin, and M. Mangolini, "Fusion of satellite images of different spatial resolutions: Assessing the quality of resulting images," *Photogrammetric engineering and remote sensing*, vol. 63, no. 6, pp. 691–699, 1997.
- [67] B. Aiazzi, L. Alparone, S. Baronti, and A. Garzelli, "Context-driven fusion of high spatial and spectral resolution images based on oversampled multiresolution analysis," *IEEE Transactions on geoscience and remote sensing*, vol. 40, no. 10, pp. 2300–2312, 2002.
- [68] S. Lolli, L. Alparone, A. Garzelli, and G. Vivone, "Haze correction for contrast-based multispectral pansharpening," *IEEE Geoscience and Remote Sensing Letters*, vol. 14, no. 12, pp. 2255–2259, 2017.
- [69] G. Vivone, "Robust band-dependent spatial-detail approaches for panchromatic sharpening," *IEEE transactions on Geoscience and Remote Sensing*, vol. 57, no. 9, pp. 6421–6433, 2019.
- [70] G. Vivone, R. Restaino, and J. Chanussot, "Full scale regression-based injection coefficients for panchromatic sharpening," *IEEE Transactions on Image Processing*, vol. 27, no. 7, pp. 3418–3431, 2018.
- [71] Q. Yuan, Y. Wei, X. Meng, H. Shen, and L. Zhang, "A multiscale and multidepth convolutional neural network for remote sensing imagery pan-sharpening," *IEEE Journal of Selected Topics in Applied Earth Observations and Remote Sensing*, vol. 11, no. 3, pp. 978–989, 2018.
- [72] X. Wu, T.-Z. Huang, L.-J. Deng, and T.-J. Zhang, "Dynamic cross feature fusion for remote sensing pansharpening," in *Proceedings of the IEEE/CVF International Conference on Computer Vision*, 2021, pp. 14 687–14 696.
- [73] S. Li, R. Dian, L. Fang, and J. M. Bioucas-Dias, "Fusing hyperspectral and multispectral images via coupled sparse tensor factorization," *IEEE Transactions on Image Processing*, vol. 27, no. 8, pp. 4118–4130, 2018.
- [74] Q. Wei, N. Dobigeon, and J.-Y. Tournet, "Fast fusion of multi-band images based on solving a Sylvester equation," *IEEE Transactions on Image Processing*, vol. 24, no. 11, pp. 4109–4121, 2015.
- [75] T. Xu, T.-Z. Huang, L.-J. Deng, and N. Yokoya, "An iterative regularization method based on tensor subspace representation for hyperspectral image super-resolution," *IEEE Transactions on Geoscience and Remote Sensing*, vol. 60, pp. 1–16, 2022.
- [76] R. Dian, S. Li, and L. Fang, "Learning a low tensor-train rank representation for hyperspectral image super-resolution," *IEEE Transactions on*

- Neural Networks and Learning Systems*, vol. 30, no. 9, pp. 2672–2683, 2019.
- [77] R. Dian and S. Li, “Hyperspectral image super-resolution via subspace-based low tensor multi-rank regularization,” *IEEE Transactions on Image Processing*, vol. 28, no. 10, pp. 5135–5146, 2019.
 - [78] X. Zhang, W. Huang, Q. Wang, and X. Li, “Ssr-net: Spatial-spectral reconstruction network for hyperspectral and multispectral image fusion,” *IEEE Transactions on Geoscience and Remote Sensing*, vol. 59, no. 7, pp. 5953–5965, 2020.
 - [79] X. Liu, Q. Liu, and Y. Wang, “Remote sensing image fusion based on two-stream fusion network,” *Information Fusion*, vol. 55, pp. 1–15, 2020.
 - [80] J.-F. Hu, T.-Z. Huang, L.-J. Deng, H.-X. Dou, D. Hong, and G. Vivone, “Fusformer: A transformer-based fusion network for hyperspectral image super-resolution,” *IEEE Geoscience and Remote Sensing Letters*, vol. 19, pp. 1–5, 2022.
 - [81] J.-F. Hu, T.-Z. Huang, L.-J. Deng, T.-X. Jiang, G. Vivone, and J. Chanussot, “Hyperspectral image super-resolution via deep spatio-spectral attention convolutional neural networks,” *IEEE Transactions on Neural Networks and Learning Systems*, vol. 33, no. 12, pp. 7251–7265, 2021.
 - [82] T. Huang, W. Dong, J. Wu, L. Li, X. Li, and G. Shi, “Deep hyperspectral image fusion network with iterative spatio-spectral regularization,” *IEEE Transactions on Computational Imaging*, vol. 8, pp. 201–214, 2022.
 - [83] R. H. Yuhas, A. F. Goetz, and J. W. Boardman, “Discrimination among semi-arid landscape endmembers using the spectral angle mapper (sam) algorithm,” in *JPL, Summaries of the Third Annual JPL Airborne Geoscience Workshop. Volume 1: AVIRIS Workshop*, 1992.
 - [84] L. Wald, *Data fusion: definitions and architectures: fusion of images of different spatial resolutions*. Presses des MINES, 2002.
 - [85] J. T. Zhou, D. L. Civco, and J. A. Silander, “A wavelet transform method to merge landsat tm and spot panchromatic data,” *International Journal of Remote Sensing*, vol. 19, pp. 743–757, 1998.
 - [86] J. Zhou, D. L. Civco, and J. A. Silander, “A wavelet transform method to merge landsat tm and spot panchromatic data,” *International journal of remote sensing*, vol. 19, no. 4, pp. 743–757, 1998.
 - [87] G. Vivone, L. Alparone, J. Chanussot, M. Dalla Mura, A. Garzelli, G. A. Licciardi, R. Restaino, and L. Wald, “A critical comparison among pansharpening algorithms,” *IEEE Transactions on Geoscience and Remote Sensing*, vol. 53, no. 5, pp. 2565–2586, 2014.
 - [88] Z. Wang, A. C. Bovik, H. R. Sheikh, and E. P. Simoncelli, “Image quality assessment: from error visibility to structural similarity,” *IEEE transactions on image processing*, vol. 13, no. 4, pp. 600–612, 2004.
 - [89] A. C. Li, M. Prabhudesai, S. Duggal, E. Brown, and D. Pathak, “Your diffusion model is secretly a zero-shot classifier,” *arXiv preprint arXiv:2303.16203*, 2023.
 - [90] W. Wu, Y. Zhao, M. Z. Shou, H. Zhou, and C. Shen, “Diffumask: Synthesizing images with pixel-level annotations for semantic segmentation using diffusion models,” *arXiv preprint arXiv:2303.11681*, 2023.
 - [91] P. Dhariwal and A. Nichol, “Diffusion models beat gans on image synthesis,” *Advances in Neural Information Processing Systems*, vol. 34, pp. 8780–8794, 2021.
 - [92] L. Zhang and M. Agrawala, “Adding conditional control to text-to-image diffusion models,” *arXiv preprint arXiv:2302.05543*, 2023.